

# Idealized large-eddy simulations of stratocumulus advecting over cold water. Part 1: Boundary layer decoupling

Youtong Zheng<sup>1</sup>, Haipeng Zhang<sup>1</sup>, Daniel Rosenfeld<sup>2</sup>, Seoung-Soo Lee<sup>1</sup>, Tianning Su<sup>1</sup>, and Zhanqing Li<sup>1</sup>

<sup>1</sup>University of Maryland

<sup>2</sup>Herew University of Jerusalem

November 24, 2022

## Abstract

We explore the decoupling physics of a stratocumulus-topped boundary layer (STBL) moving over cooler water, a situation mimicking the warm air advection (WADV). We simulate an initially well-mixed STBL over a doubly periodic domain with the sea surface temperature decreasing linearly over time using the System for Atmospheric Modeling large-eddy model. Due to the surface cooling, the STBL becomes increasingly stably stratified, manifested as a near-surface temperature inversion topped by a well-mixed cloud-containing layer. Unlike the stably stratified STBL in cold air advection (CADV) that is characterized by cumulus coupling, the stratocumulus deck in the WADV is unambiguously decoupled from the sea surface, manifested as weakly negative buoyancy flux throughout the sub-cloud layer. Without the influxes of buoyancy from the surface, the convective circulation in the well-mixed cloud-containing layer is driven by cloud-top radiative cooling. In such a regime, the downdrafts propel the circulation, in contrast to that in CADV regime for which the cumulus updrafts play a more determinant role. Such a contrast in convection regime explains the difference in many aspects of the STBLs including the entrainment rate, cloud homogeneity, vertical exchanges of heat and moisture, and lifetime of the stratocumulus deck, with the last being subject to a more thorough investigation in part 2 of this study. Finally, we investigate under what conditions a secondary stratus near the surface (or fog) can form in the WADV. We found that weaker subsidence favors the formation of fog whereas a more rapid surface cooling rate doesn't.



20 **Abstract**

21 We explore the decoupling physics of a stratocumulus-topped boundary layer (STBL) moving  
22 over cooler water, a situation mimicking the warm air advection (WADV). We simulate an  
23 initially well-mixed STBL over a doubly periodic domain with the sea surface temperature  
24 decreasing linearly over time using the System for Atmospheric Modeling large-eddy model.  
25 Due to the surface cooling, the STBL becomes increasingly stably stratified, manifested as a  
26 near-surface temperature inversion topped by a well-mixed cloud-containing layer. Unlike the  
27 stably stratified STBL in cold air advection (CADV) that is characterized by cumulus coupling,  
28 the stratocumulus deck in the WADV is unambiguously decoupled from the sea surface,  
29 manifested as weakly negative buoyancy flux throughout the sub-cloud layer. Without the  
30 influxes of buoyancy from the surface, the convective circulation in the well-mixed cloud-  
31 containing layer is driven by cloud-top radiative cooling. In such a regime, the downdrafts propel  
32 the circulation, in contrast to that in CADV regime for which the cumulus updrafts play a more  
33 determinant role. Such a contrast in convection regime explains the difference in many aspects of  
34 the STBLs including the entrainment rate, cloud homogeneity, vertical exchanges of heat and  
35 moisture, and lifetime of the stratocumulus deck, with the last being subject to a more thorough  
36 investigation in part 2 of this study. Finally, we investigate under what conditions a secondary  
37 stratus near the surface (or fog) can form in the WADV. We found that weaker subsidence favors  
38 the formation of fog whereas a more rapid surface cooling rate doesn't.

39

40

41

42 **Significant statement**

43 The low-lying blanket-like clouds, called stratocumulus (Sc), reflect much incoming sunlight,  
44 substantially modulating the Earth's temperature. While much is known about how the Sc  
45 evolves when it moves over warmer water, few studies examine the opposite situation of Sc  
46 moving over colder water. We used a high-resolution numerical model to simulate such a case.  
47 When moving over cold water, the Sc becomes unambiguously decoupled from the water surface,  
48 distinctive from its warm counterpart in which the Sc interacts with the water surface via  
49 intermittent cauliflower-like clouds called cumulus clouds. Such decoupling influences many  
50 aspects of the Sc-sea-surface system, which combine to alter the ability of the Sc to reflect  
51 sunlight, thereby influencing the climate. This work laid the foundation for future work that  
52 quantifies the contribution of such a decoupled Sc regime to the Earth's radiative budget and  
53 climate change.

54

55

56

57

58

59

60

61

## 62 1. Introduction

63 Marine stratocumulus (Sc) significantly alters the Earth's radiative budgets at both the  
64 surface and the top of the atmosphere (Hartmann et al., 1992; Hahn and Warren, 2007; Wood,  
65 2012). The Sc strongly interacts with the marine boundary layer. The interactions manifest as  
66 exchanges of heat, moisture, and mass between the stratocumulus and the sea surface, forming a  
67 coupled Sc-surface system commonly known as the stratocumulus-topped planetary boundary  
68 layer (STBL). The earliest credible description of the STBL physics is Lilly (1968)'s mixed-  
69 layer model. The model treats the column of air from the surface to the top of Sc as a well-mixed  
70 bulk layer and parameterizes basic cloud physics and fluxes (i.e. energy, moisture, and mass).  
71 The model succeeds in explaining a series of important behaviors of STBL over the subtropical  
72 oceans such as the STBL response to large-scale environment (Schubert et al., 1979a, b;  
73 Wakefield and Schubert, 1981; Stevens, 2006), the STBL decoupling during the cloud regime  
74 transition (Bretherton and Wyant, 1997; Zheng et al., 2020), diurnal cycle (Caldwell et al., 2005;  
75 Zhang et al., 2005), dominant time scales (Jones et al., 2014), slow manifold behavior  
76 (Bretherton et al., 2010), and aerosol influences on Sc (Wood, 2007; Caldwell and Bretherton,  
77 2009; Uchida et al., 2010).

78 The Lily's mixed-layer model becomes invalid if the STBL stably stratifies, a phenomenon  
79 widely known as STBL decoupling (Nicholl, 1984). The decoupling physics can be understood  
80 from the perspective of boundary layer energetics. In a well-mixed STBL over cold water, air  
81 parcels entrained from the overlying inversion are cooled by thermal radiation at the cloud top,  
82 sinking through the boundary layer. This well-mixed state is sustained by a rough balance  
83 between entrainment warming and radiative cooling in the upper part of the STBL. When the  
84 warming outweighs the cooling, the entrained warm airs are too light to sink, leading to the

85 stable stratification of the boundary layer. Examples include the decoupling during the  
86 subtropical stratocumulus-to-cumulus transition due to enhanced entrainment warming  
87 (Bretherton and Wyant, 1997), decoupling by precipitation that warms the cloud layer (Nicholls,  
88 1984; Stevens et al., 1998), and daytime decoupling by solar insolation that weakens cloud-top  
89 radiative cooling (Nicholls and Leighton, 1986; Zheng et al., 2018).

90 The above decoupling mechanisms have been studied in subtropical conditions where the  
91 trade winds advect the STBL toward the equator with warmer surfaces. The cold air advection  
92 builds up the potential energy of the environment so that the decoupled STBLs are typically  
93 conditionally unstable. This allows for the development of cumulus (Cu) that often penetrates the  
94 Sc decks, forming Cu-coupled STBLs. In such a cloud regime, the Sc can interact with the  
95 surface through the conduits of the Cu convection so that whether or not to call the boundary  
96 layer “decoupled” has been controversial (Miller and Albrecht, 1995; Stevens et al., 1998; Goren  
97 et al., 2018a; Zheng et al., 2018; Zheng and Li, 2019).

98 To reconcile the controversy, Zheng et al. (2020) added a new dimension, namely low-  
99 level temperature advection, to the problem. Zheng et al. (2020) considered the coupling state of  
100 STBL in a spectrum of low-level temperature advection ranging from the extremely cold air  
101 advection such as cold air outbreaks to the warm air advection in the warm sector of mid-latitude  
102 cyclones. The STBLs embedded in cold air advection flows are either fully coupled (i.e. well-  
103 mixed) or Cu-coupled. The unambiguously decoupled STBLs only occur in warm air advection  
104 conditions where the stable stratification is sufficiently strong to prohibit the cumulus coupling.  
105 This view is supported by ground-based observations from the Southern Ocean, northeast  
106 subtropical Pacific, and northeast Atlantic. These observations show that, as the low-level flow

107 shifts from cold to warm air advection, the boundary layer turns from a Cu-coupled STBL to a  
108 considerably stably stratified STBL without Cu coupling (i.e. unambiguously decoupled STBL).

109 Poorly understood is the unambiguously decoupled STBLs experiencing warm advection.  
110 In contrast to Cu-coupled STBLs, typical at subtropics, the STBLs under warm advection  
111 conditions receive scarce attention despite their potential abundance in midlatitudes (Agee, 1987;  
112 Fletcher et al., 2016; Wall et al., 2017; Scott et al., 2020). This motivates the current study. We  
113 aim to elucidate the physics of STBL response to warm advection using idealized large-eddy  
114 simulations. By the “idealized”, we mean simulating an STBL over a doubly periodic domain  
115 with the sea surface temperature (SST) decreasing over time to mimic the influences of warm air  
116 advection. This idealized setup is the same as the conventional LES studies of Sc-to-Cu  
117 transitions (Sandu and Stevens, 2011; Van der Dussen et al., 2013; Bretherton and Blossey,  
118 2014), in which the SST increases over time. Such consistency allows for direct comparisons.

119 In addition to further the understanding of decoupling dynamics, another motivation is a  
120 lack of consensus on the role of horizontal temperature advection on low cloud radiative effects.  
121 Prior observations show that marine low clouds are considerably fewer and thinner under  
122 warmer air advection conditions (Norris and Iacobellis, 2005; Myers and Norris, 2015; Klein et  
123 al., 2017; Scott et al., 2020). Their interpretation is that the warm-advection-induced decoupling  
124 leads to less moisture supply from the sea surface to the clouds, thereby thinning the clouds.  
125 Contrasting pieces of evidence, however, exist. For example, Zheng and Li (2019) found that  
126 clouds can be very persistent even if they are decoupled from the sea surface under warm  
127 advection conditions, as shown by geostationary satellite images and ship-based remote sensing  
128 data. This finding is consistent with Goren et al. (2018b) who found that precipitating marine  
129 clouds are more persistent in decoupled STBLs than coupled ones. Moreover, some studies show

130 no statistically significant dependence of low cloud radiative effects on temperature advection in  
131 climate models (personal communications with Daniel McCoy) and ground-based observations  
132 over mid-latitude oceans (Naud et al., 2020). The mixed lines of evidence suggest a lack of  
133 understanding of the mechanism underlying the low cloud response to warm air advection.

134 In summary, this study attempts to elucidate the physical mechanisms of warm-advection-  
135 induced decoupling (part 1) and its control on low-cloud radiative effects (part 2) by using  
136 idealized large-eddy simulations. Part 1 is dedicated to decoupling dynamics whereas part 2  
137 focuses on its implications for the low cloud feedback. Although the warm air advection is our  
138 focus, our analyses are centered on comparing the results of warm air advection with the cold air  
139 advection (as the benchmark). This enables a clearer presentation of the new insights in the  
140 context of conventional knowledge. The next section introduces the LES model and the  
141 experiments. Section 3 shows the results, followed by discussions and concluding remarks.

142

## 143 **2. Large-Eddy Simulations**

### 144 2.1. Model and case descriptions

145 We use the System for Atmospheric Modeling (SAM) model, version 6.11.3  
146 (Khairoutdinov and Randall, 2003). SAM uses liquid water static energy ( $h_l$ ), total non-  
147 precipitating water mixing ratio ( $q_t$ ), and total precipitating water mixing ratio as prognostic  
148 thermodynamic scalars. We use the advection scheme developed by Smolarkiewicz and  
149 Grabowski (1990), a simplified (drizzle only) version of Khairoutdinov and Kogan (2000)'s  
150 microphysics scheme and RRTMG radiation (Iacono et al., 2008). Surface fluxes of temperature,  
151 moisture, and momentum are calculated by similarity theory.

152 We use a horizontal grid spacing of 35 m in a doubly periodic domain with a size of  $4480^2$   
153  $\text{m}^2$ . We chose such a small domain size purely for computational efficiency. It should be too  
154 small to represent mesoscale convective circulation typical for precipitating STBLs. The STBLs  
155 studied here are weakly precipitating so that the influence of mesoscale dynamics should be  
156 minor. This is confirmed by a sensitivity test for a larger domain of  $8960^2 \text{ m}^2$  that yields nearly  
157 identical results (not shown). The vertical grid spacing is set as 5 m in the cloud and inversion  
158 layer to resolve entrainment. The grid spacing stretches above  $\sim 2400$  m until the domain top of  
159  $\sim 4200$  m, which is high enough for gravity wave damping. There is a total of 512 vertical grids.

160 The base case for our simulations is the case from the Atlantic Stratocumulus Transition  
161 Experiment (ASTEX) (Albrecht et al., 1995). The ASTEX case has been a benchmark for LES  
162 simulations of the Sc-to-Cu transitions (Van der Dussen et al., 2013). A unique aspect of the  
163 ASTEX case is that observations from an aircraft and balloons are “Lagrangian” for they follow  
164 the evolution of STBL air mass. This is particularly important for simulating the STBL response  
165 to horizontal temperature advection, for which the SST evolution along the air mass trajectory is  
166 the key driver. During the ASTEX, the SST increases by  $\sim 4$  K over the 40-hour simulation of  
167 the ASTEX case. Such an increase in SST is widely regarded as the determinant driver of the  
168 cloud regime transition.

169 As stated in the introduction, we use a cold air advection case as a benchmark for  
170 understanding the role of warm advection. To that end, we conduct two idealized experiments by  
171 simplifying the forcing of the original ASTEX case. In the first experiment, we linearize the SST  
172 increase rate, yielding an SST increasing rate of 2.6 K/day (named “CADV”). In the second  
173 experiment, we decrease the SST by 2.6 K/day to mimic the influence of warm air advection

174 (named “WADV”). All other initial and forcing conditions are the same (see Van der Dussen et  
175 al., 2013 for the detail).

176 The WADV run is highly idealized. In the real world, the low-level horizontal temperature  
177 advection strongly couples with other synoptic variables. For example, warm air advection  
178 typically co-occurs with large-scale ascent motions whereas cold air advection is more likely to  
179 occur in a subsiding atmosphere (Holton, 1973; Norris and Klein, 2000; Zheng et al., 2020). In  
180 that regard, it is unrealistic that the CADV and WADV experience the same large-scale forcing.  
181 But, the purpose of this study is not to reproduce the real-world STBLs, but to understand the  
182 most essential physics behind the problem. All the existing hypotheses for STBL response to  
183 warm air advection are centered on the stabilization effect of warm advection as the most  
184 determinant process (Norris and Iacobellis, 2005; Klein et al., 2017; Scott et al., 2020). In other  
185 words, our current level of understanding does not allow for formulating a hypothesis  
186 sophisticated enough to account for every aspect of the problem. Thus, we consider our  
187 simulations a starting point for future more realistic numerical explorations.

## 188 2.2. Diagnostic statistics

189 The boundary layer height ( $z_i$ ) and heights of capping inversion base and top are  
190 determined using the method developed by Yamaguchi and Randall (2011) that is based on the  
191 geometry of  $h_l$  variance. This allows us to compute the buoyancy jump across the inversion,  
192 which will be used to quantify the entrainment-driven decoupling shown later. We quantify the  
193 degree of stratification of an STBL using the  $h_l$  averaged over the top 10% of the  $z_i$  minus the  $h_l$   
194 averaged over the bottom 10% of the  $z_i$ , marked as  $\Delta_{BL} h_l$ .

195 We determine the lifting condensation level (LCL) using the exact analytic formula  
196 developed by Romps (2017). The entrainment rate ( $w_e$ ) is determined using the boundary layer  
197 mass budget equation:  $w_e = dz_i/dt - w_{sub}$ , in which the  $w_{sub}$  is the large-scale subsidence rate at  
198 the boundary layer top.

199

### 200 **3. Results**

#### 201 3.1. Time evolution

202 Figures 2 and 3 show the time evolution of selected outputs, which illustrate many  
203 characteristics of the STBL under the influence of warm air advection. The warm air advection  
204 substantially suppresses the surface latent and sensible heat fluxes (Figs. 2a and b). This lowers  
205 the turbulence level of the boundary layer, weakens the entrainment near the boundary layer top  
206 (Fig. 2d), and slows the deepening (or even shallowing) of the boundary layer (Fig. 2c). Such a  
207 contrast in surface fluxes, as will be evident later, is the most essential factor explaining most of  
208 the differences between the two simulations.

209 Figures 3a and b show the time-height plots of the cloud fraction for the two runs. The  
210 CADV presents a textbook-like Sc-to-Cu transition whereas the WADV shows a solid Sc deck  
211 persistent throughout the simulation. The persistence is primarily due to the weak entrainment  
212 drying, discussed in detail in part 2 (Zhang et al., 2021). Because the focus of this study is the  
213 boundary layer decoupling, we look at time evolution of  $h_l$  and  $q_l$  profiles (Figures 3 c-f). Both  
214 regimes show increasingly stably stratified boundary layers, but their geometries of stratification  
215 differ greatly, which can be more clearly seen from the sounding at a selected time of  $t = 30$  h  
216 (Fig. 4). In CADV, the boundary layer is stratified into two well-mixed layers: the upper cloud-

217 containing layer driven by radiative cooling and the bottom layer driven by surface heating.  
 218 These two layers are separated by a weakly stratified layer. In WADV, however, the  
 219 stratification concentrates near the surface, as seen from a well-defined temperature inversion in  
 220 the lowest quarter of the boundary layer. Above the inversion is a well-mixed cloud-containing  
 221 layer. The convection in this mixed-layer is driven by cloud-top radiative cooling, suggested by  
 222 the top-heavy structure of vertical velocity variance (Fig. 3h and Fig. 4c) and the negative  
 223 vertical velocity skewness (Fig. 3j), an indicator of top-driven convection (Moeng and Rotunno,  
 224 1990).

225 The above analysis dictates two different decoupling mechanisms: entrainment-warming-  
 226 driven decoupling in CADV and surface-cooling-driven decoupling in WADV. This statement  
 227 can be demonstrated by quantifying the role of entrainment warming in decoupling. Here we use  
 228 a model diagnostic called “excess entrainment warming” (EEW), developed by Zheng et al.  
 229 (2021). The EEW is defined as:

$$230 \quad EEW = \underbrace{\rho C_p w_e \Delta_{inv} \theta_v}_{\text{Entrainment warming}} + \underbrace{\Delta_{cld} F_{rad} + \rho L_v \Delta_{cld} F_{prec}}_{\text{Diabatic cooling}}, \quad (1)$$

231 where  $\rho$  is the air density,  $C_p$  is the specific heat of air,  $L_v$  is the latent heat of evaporation of  
 232 water,  $F_{rad}$  is the radiative flux ( $\text{W m}^{-2}$ ), and  $F_{prec}$  is the precipitation flux ( $\text{m}^{-1}$ ). The symbol  
 233 “ $\Delta_{cld}$ ” represents the divergence across the Sc cloud layer. A larger EEW means that the diabatic  
 234 cooling (radiative cooling compromised by precipitation-induced heating) is not sufficient to  
 235 balance the entrainment warming so that the entrained air is not cold enough to be sink through  
 236 the sub-cloud layer. This causes the accumulation of warm air in the upper boundary layer,  
 237 stably stratifying the STBL. A small or even negative value means that the entrainment-induced  
 238 warming is balanced by the diabatic cooling, preventing the decoupling. Figure 2g shows the

239 evolution of EEW for the two experiments. The CADV has an EEW of several tens of  $\text{W m}^{-2}$   
240 throughout the two simulations, suggesting that entrainment warming considerably outweighs  
241 the diabatic cooling. On the contrary, the EEW remains negative most of the time in WADV,  
242 demonstrating a minimal role of entrainment in the decoupling.

243         Given that the entrainment cannot explain the decoupling in WADV, the near-surface  
244 cooling is the dominant decoupling factor. To understand what drives the near-surface cooling in  
245 WADV, we analyze the budgets of  $\frac{dh_t}{dt}$  in the lowest 200 m when the cooling is most distinctive.  
246 We found that the turbulent transport,  $(\frac{dh_t}{dt})_{tur}$ , and radiation,  $(\frac{dh_t}{dt})_{rad}$ , are the dominant  
247 controllers, which can be illustrated in Figure 5. The cooling effect of turbulent transport is  
248 straightforward to understand. In WADV, except at the beginning, boundary layer air is notably  
249 warmer than the SST (Fig. 2g), leading to the downward loss of heat to the sea surface. This  
250 causes cooling of the bottom boundary layer. However, turbulent transport is not the only  
251 cooling mechanism, as seen from the thin layer of turbulent warming in the lowest few tens of  
252 meters (Fig. 5b).

253         The thin layer of turbulent warming can be explained by the turbulence adjustment to the  
254 near-surface radiative cooling (Fig. 5c). What causes the abnormally large radiative cooling near  
255 the surface? According to the conventional knowledge about radiative transfer, we know that  
256 atmospheric radiative cooling has three contributing components: (1) exchange of radiative  
257 energy with underlying atmosphere, (2) exchange of radiative energy with overlying atmosphere,  
258 and (3) radiative energy escaping to the cold space. In a typical atmosphere where temperature  
259 decreases with altitude, the first two components roughly cancel each other, leaving the  
260 “cooling-to-space” component the dominant one (Petty, 2006). This is not the case here for the

261 air near the surface: both the overlying and underlying airs are cooler (Fig. 4a). Thus, exchanges  
262 of radiative energy in both directions cause loss of energy, considerably increasing the radiative  
263 cooling. Such a local cooling induces local convergence of turbulent flux as an adjustment  
264 process.

265 The aggregate role of the radiation and turbulence,  $(\frac{dh_l}{dt})_{tur+rad}$ , is a cooling effect. The  
266  $(\frac{dh_l}{dt})_{tur+rad}$  (Fig. 5d) bears a similarity with the  $\frac{dh_l}{dt}$  (Fig. 5a), suggesting that the two  
267 processes can explain the bulk of the near-surface cooling. The remaining difference is due to the  
268 precipitation and large-scale transport, which play a secondary role.

269 In summary, the stable stratifications of STBLs in CADV and WADV are explained by  
270 entrainment-induced warming and near-surface cooling (by turbulence and radiation),  
271 respectively. These two decoupling mechanisms can be conceptualized into a decoupling dipole:  
272 top-warming-driven versus bottom-cooling-driven decoupling.

273

### 274 3.2. The already decoupled phase

275 We have discussed processes leading to the decoupling in both regimes. Now we  
276 characterize the turbulent properties of STBLs in their already decoupled phases. Strictly  
277 speaking, there is no such thing as an equilibrium phase in our simulations because the SST  
278 keeps evolving and the STBL keeps responding. Here, we take model outputs at  $t = 30$  h as  
279 representations of already decoupled STBLs for the two regimes. One justification for selecting  $t$   
280  $= 30$  h is that the stratification degree at CADV already saturates at  $t = 30$  h, suggesting a quasi-  
281 equilibrium state (Fig. 2e). In WADV, the STBL is still stratifying, but the qualitative

282 characteristics of the STBL (e.g. thermodynamic structure, turbulence, and cloud properties)  
283 remain similar throughout the simulations. Selecting different times of the WADV run does not  
284 influence the main conclusion of this paper.

285 We first look at the three-dimensional (3D) visualization of the STBLs at  $t = 30$  h (Figure  
286 6). To more clearly visualize the cloud-surface decoupling, we show the surface plots of the  
287 near-surface  $q_t$ , defined as the top 1% of  $q_t$  in the vertical (dark red surface). The CADV regime  
288 is characterized by intermittent Cu clouds penetrating the Sc deck, known as the Cu-coupled  
289 STBL. The contour of the near-surface  $q_t$  extends vertically from the surface to the base of Cu.  
290 Through the conduit of Cu, the water from the sea surface feeds into the Sc deck. Such a feeding  
291 effect is absent in WADV. In WADV, there is only a single layer of solid Sc deck, completely  
292 separate from the surface humid air trapped near the surface. We provide movies of 2-D fluid  
293 visualization for the two runs to aid in intuitively understanding the results (see Animations 1  
294 and 2 in the supplemental material).

295 Such a difference in the cloud-surface interaction is augmented by vertical velocity fields  
296 at different levels. Figure 7 shows the vertical velocity at  $z = 10$  m (left),  $z = 0.5z_b$  (middle), and  
297  $z = z_b$  (right). The turbulent flow near the surface of the CADV regime is elongated, consistent  
298 with the typical flow structure in convective boundary layers (Moeng and Rotunno, 1990). In  
299 WADV, however, the flow is more random with a less evident elongated pattern, typical for  
300 stratified flows (Mahrt, 2014). At  $z = 0.5z_b$  in the CADV, small patches of isolated updrafts  
301 (blobs of red colors) start to emerge. These updraft regions are more humid than the surrounding  
302 regions. This pattern resembles the typical “cumulus-like” convection: moist, narrow, and strong  
303 updrafts surrounded by drier, wider, and weaker subsidence (Bjerknes, 1938). This is further  
304 supported by the positive skewness of vertical velocity, characteristic of surface-driven

305 convection (Figure 7h). In WADV, however, the “cumulus-like” convection is absent, as seen  
306 from a lack of concentrated updrafts. The skewness of vertical velocity is negative (Figure 7h),  
307 suggesting a dominance of top-cooling-driven turbulence (Wyngaard, 1987; Moeng and Rotunno,  
308 1990). Such a contrast in turbulence regime persists at  $z = z_b$ .

309 The flow visualizations (Figs 6 and 7) suggest two distinctive convection regimes:  
310 surface-heating-driven cumulus-like convection for CADV versus top-cooling-driven  
311 stratocumulus-like convection for WADV. Such a difference can be more directly seen by  
312 conditionally sampling the parcels in rising ( $w > 0$ ) and sinking motions ( $w < 0$ ) (Fig. 8a). Fig.  
313 8a shows that the vertical velocity variance is considerably stronger for updrafts than downdrafts  
314 in CADV, suggesting a more determinant role of updrafts in driving the vertical mixing, whereas  
315 the opposite is true for WADV. Note that the cloud-top radiative cooling still contributes to  
316 driving the convection in the CADV, as seen from the local maxima of vertical velocity variance  
317 in the upper Sc layer. But even in such a Sc layer, the updrafts contribute more to the turbulence  
318 via penetration of the Cu convection.

319 The relative strength of updrafts and downdrafts makes a substantial difference to how  
320 heat and moisture are transported in the vertical (Figs. 8b,c). In CADV, the vertical transport of  
321 moisture is realized by updrafts that carry humidity from the sea surface upward, feeding the Sc  
322 deck (Fig. 8b). In contrast, in the WADV, the downdrafts play a more dominant role in the  
323 vertical exchange of moisture: downdrafts transport entrained dry air toward the surface. At  $z =$   
324  $z_b$  of WADV, the supply of moisture via updrafts is close to zero, suggesting that the Sc deck  
325 almost entirely decouples from the source of humidity from below.

326           A similar conclusion can be drawn from the heat flux (Fig. 8c). The heat flux profile is  
327 relatively more complex due to the influences of diabatic heating/cooling (i.e. radiation and  
328 precipitation) to which the turbulent flux must adjust (Stevens et al., 1998). Hence we focus on  
329 the sub-cloud layer where the diabatic heating/cooling is minimal. Both regimes show a  
330 downward transport of heat, but the transport in CADV is realized by updrafts, whereas, in  
331 WADV, the downdrafts drive the downward transports of warm entrained air.

332           In addition to the profiles of heat and moisture fluxes, it is informative to look at the  
333 buoyancy flux that dictates boundary layer energetics (Fig. 8d). In CADV, the buoyancy flux is  
334 mostly positive except near the LCL. Such a structure of buoyancy profile is consistent with the  
335 conventional wisdom based on the argument of hypothetical parcel trajectory (see Bretherton et  
336 al., 1997 for detail). Again, the updrafts dominate the positive buoyant flux (light air rises),  
337 converting the potential energy of the environment to turbulent kinetic energy. Such a large  
338 buoyancy for updrafts is largely contributed by the water vapor. As seen in Fig. 8c, the heat flux  
339 for updrafts is negative throughout most of the boundary layer, which suggests cooler air  
340 ascending. The buoyancy of the ascending cool air stems from the water vapor, as seen from the  
341 strong  $q_t$  flux in updrafts (Fig. 8b). In WADV, however, the cloud-layer and sub-cloud layer  
342 exhibit opposite signs. In the cloud-layer, the buoyancy flux is positive, contributed by both  
343 updrafts and downdrafts through latent heating and diabatic cooling, respectively. The  
344 downdrafts, again, contribute more. In the sub-cloud layer, the buoyancy flux is slightly negative.  
345 Such a dipole-like geometry of buoyancy flux profile resembles that of the heat flux (Fig. 8c),  
346 suggesting the contribution of buoyancy from water vapor is insignificant, especially in the sub-  
347 cloud layer.

348           So what drives the downward motion of the warm air if the water vapor effect does not  
349 contribute? From the perspective of the heat budget constraint, the warm air must descend  
350 somewhere in the sub-cloud layer in order to transfer heat from the atmosphere into the sea  
351 surface, a necessary consequence of WADV (warm air overlying cold surface). Then, what are  
352 the underlying mechanisms? We explain it using the argument from Schubert et al. (1979a) who  
353 stress the role of the pressure field. The central idea is that the pressure gradient force propels the  
354 air overturning, which overcomes the negative buoyancy. This effect can be more clearly  
355 illustrated by the  $\overline{w'p'}$  profile of the WADV experiment (Fig. 9). The  $\overline{w'p'}$  is negative in the  
356 sub-cloud layer for both updrafts and downdrafts. This suggests that air rises in low-pressure  
357 regions and sinks in high-pressure regions, typical for pressure-driven air overturning. The  
358 negative  $\overline{w'p'}$  at the cloud base suggests that the cloud layer does work to the sub-cloud layer,  
359 pumping up the sub-cloud air, completing the circulation. This process is consistent with the idea  
360 of boundary layer energetics. As the boundary layer being stabilized by the warm air advection,  
361 the turbulence generated from the cloud-top radiative cooling must work against the stability to  
362 well mix the boundary layer. This is a process that converts turbulent energy to the potential  
363 energy of the environment. Such an energy conversion is realized by the descending of warm air,  
364 propelled by the pressure gradient.

365

### 366 3.3. On the formation of double-layer stratiform clouds

367           From observations, under warm air advection conditions, often found are double-layer  
368 stratiform clouds, with the upper layer capped by the major temperature inversion and the lower  
369 layer close to the surface, often manifested as fog (Zheng et al., 2020) (personal communications

370 with Mark Smalley and Steven Klein). Such a double-layer cloud regime is distinctive from the  
371 Cu-fed Sc because the lower clouds are stratiform, not cumuliform. It is, thus, important to  
372 understand why our WADV experiment does not develop a stratus near surface.

373 A hypothesis that naturally arises is that, in the WADV run, the near-surface temperature  
374 inversion is not sufficiently strong to sustain high humidity (by trapping water vapor within it).  
375 To test this hypothesis, we run additional simulations by altering the forcing parameters for the  
376 WADV. First, we double the  $T_{adv}$  from 2.6 K/day to 5.2 K/day, denoted as “WADV5.2”. The  
377 expectation is that if the SST cools rapidly enough, the near-surface inversion may be strong  
378 enough to form fogs. Second, we decrease the large-scale divergence from  $5 \times 10^{-6}$  to  $3 \times 10^{-6}$ ,  
379 denoted as “WADV Div3”. We expect that, for weaker subsidence, the boundary layer deepens  
380 more rapidly, enhancing the warming of the upper boundary layer, which strengthens the near-  
381 surface temperature inversion.

382 Figure 10 shows the cross-sections of cloudiness of the two experiments. A double-layer  
383 stratiform cloud emerges in the WADV Div3, but not in WADV5.2 (only a tiny amount of small  
384 clouds below the Sc deck). The bottom panel of Fig. 10 shows the sounding at  $t = 30$  h. The  
385 filled circles mark the heights of the near-surface temperature inversion,  $z_{li}$ , determined as the  
386 level of the local maxima of liquid water potential temperature variance (Yamaguchi and Randall,  
387 2008). We find that both new experiments generate stronger near-surface inversions than the  
388 WADV (Fig. 10c), consistent with our expectations. However, a strong temperature inversion  
389 does not necessarily increase the  $q_i$ : relative to WADV, the  $q_i$  within the inversion is higher in  
390 WADV Div3, but lower in WADV5.2 (Fig. 10d). For this reason, the WADV5.2 does not  
391 develop enough high RH to form a cloud (Fig. 10e).

392 To understand what drives the difference in the  $q_t$ , we consider the atmosphere from the  
 393 surface to the  $z_{li}$  as a bulk layer and take the  $\overline{w'q'_t}$  at the top and bottom, denoted as  $(\overline{w'q'_t})_{top}$   
 394 and  $(\overline{w'q'_t})_{bot}$ , respectively (Fig. 11a and b). Their difference divided by the  $z_{li}$  yields the net  
 395 moistening rate of the near-surface layer (Fig. 11c). We found considerably smaller  $(\overline{w'q'_t})_{bot}$  in  
 396 WADV5.2 than the other two runs (Fig. 11b), suggesting that the downward loss of humidity is  
 397 the primary reason for its greater drying (Fig. 11c and Fig. 10d). The negative  $(\overline{w'q'_t})_{bot}$  is  
 398 driven by the more negative  $q_t$  gradient across the surface, namely  $q_{sfc}^* - q_{air}$ , where the  $q_{sfc}^*$  is the  
 399 saturation  $q_t$  of the SST and  $q_{air}$  is the  $q_t$  of the overlying air (Fig. 11d). The more negative  $q_{sfc}^* -$   
 400  $q_{air}$  is fundamentally constrained by the Clausiuou-Clapeyron relationship. Unlike the WADV5.2,  
 401 the WADV Div 3 does not experience any changes in the  $(\overline{w'q'_t})_{bot}$  compared with the WADV.  
 402 Instead, the  $(\overline{w'q'_t})_{top}$  becomes markedly smaller than that of the WADV<sup>1</sup>. This means less  
 403 upward loss of moisture, thereby elevating the  $q_t$  relative to the WADV.

404 In summary, weaker subsidence favors the emergence of double-layer stratiform clouds  
 405 because weaker subsidence allows for more rapid boundary layer deepening, which warms the  
 406 upper boundary layer, enhancing the temperature inversion in the lower boundary layer. The  
 407 stronger temperature inversion traps the moisture within, eventually elevating the RH to unity.  
 408 Stronger warm advection (i.e. more rapid sea surface cooling) does not necessarily favor the  
 409 formation of such secondary stratus because a cooler sea surface facilitates the downward  
 410 transport of moisture from the atmosphere into the sea. This acts to dry the near-surface air,  
 411 preventing the formation of clouds.

412

---

<sup>1</sup> The smaller  $(\overline{w'q'_t})_{top}$  is driven by the stronger near-surface temperature inversion at WADV Div3 (Fig. 10a), which inhibits the vertical exchange of moisture between the bottom and upper boundary layer.

#### 413 4. Summary

414 We have investigated the response of a stratocumulus-topped boundary layer (STBL) to a  
415 cooling sea surface by using idealized large-eddy simulations. The decreasing sea surface  
416 temperature mimics the influence of low-level warm air advection (WADV). In addition to  
417 characterizing the basic turbulence structure of the boundary layer in WADV, we are particularly  
418 interested in testing an unproven argument: an unambiguous decoupling between stratocumulus  
419 clouds and the surface can be achieved in warm air advection (WADV) flow, but not in cold  
420 advection (CADV) flow because the latter favors cumulus-induced coupling while the former  
421 doesn't (Zheng and Li, 2019; Zheng et al., 2020). To examine this argument, we investigate the  
422 decoupling physics of an STBL experiencing WADV and compare the results with that in  
423 CADV. We found the followings:

- 424 i. An STBL tends to become stably stratified in both WADV and CADV conditions,  
425 but their driving mechanism is dramatically different. The stratification in CADV is  
426 caused by the enhanced entrainment warming (i.e. the “deepening-warming” theory  
427 by Bretherton and Wyant, 1997) whereas, in WADV, it is driven by cooling of the  
428 bottom boundary layer due to radiative cooling and loss of heat to the sea surface  
429 via turbulent transport. The difference in the driving mechanism constitutes a  
430 decoupling dipole: top-warming-driven versus bottom-cooling-driven.
- 431  
432 ii. The surface cooling in the WADV causes a temperature inversion in the lower  
433 boundary layer. Above the inversion is a well-mixed cloud-containing layer whose  
434 convection is driven by the cloud-top radiative cooling. This is different from the

435 temperature structure in CADV that has two well-mixed layers separated by a  
436 conditionally unstable layer.

437  
438 iii. The difference in the boundary layer thermodynamics between WADV and CADV  
439 significantly alters the turbulence and cloud regimes. Unlike the emergence of  
440 cumulus-coupled stratocumulus in CADV, the WADV simulation manifests a  
441 single stratocumulus deck that is persistent, horizontally homogeneous, relatively  
442 quiet, and unambiguously decoupled from the moisture source of the sea surface.  
443 Such a cloud pattern is a consequence of a lack of surface fluxes, leaving the cloud-  
444 top cooling the only driver of convection.

445  
446 iv. Due to the lack of surface fluxes, the buoyancy flux profile in WADV manifests a  
447 dipole pattern: positive in the cloud layer and weakly negative in the sub-cloud  
448 layer. This, in combination with the profile of the pressure covariation with the  
449 vertical velocity, dictates that the cloud layer does work to the sub-cloud layer to  
450 pump up the air, maintaining the convective circulation. Such a cloud-containing  
451 mixed-layer, however, cannot extend down to the surface because of the strong  
452 near-surface inversion sustained by the surface cooling. This is, again, in contrast to  
453 the convective circulation in CADV that is not only driven by cloud-top cooling but  
454 also surface heating that propels strong updrafts responsible for the bulk of the heat  
455 and moisture transports.

456

457 v. A secondary stratiform cloud (or fog) can form in the lower boundary layer in  
458 WADV if the large-scale subsidence weakens. The mechanism is that the STBL  
459 deepens more rapidly if the subsidence is weaker. This leads to more effective  
460 entrainment near the STBL top, warming the boundary layer and enhancing the  
461 temperature gradient between the warm boundary layer and the cold surface. This  
462 strengthens the near-surface temperature inversion, trapping more water vapor  
463 within the layer, raising the relative humidity to unity. Interestingly, increasing the  
464 cooling rate of sea surface temperature does not necessarily cause the formation of  
465 the fog. The reason is that colder sea surface enhances the negative moisture  
466 gradient between the air in contact with the sea surface and the overlying air. This  
467 causes a more rapid loss of moisture from the near-surface air to the sea, thereby  
468 suppressing the fog formation.

469

## 470 **Acknowledgments**

471 This study is supported by the Department of Energy (DOE) Atmospheric System Research  
472 program (DE-SC0018996). S. S. Lee is also supported by the National Research Foundation of  
473 Korea (NRF) grant funded by the South Korean government (MSIT) (grant no.  
474 NRF2020R1A2C1003215). The SAM model code is available at  
475 <http://rossby.msrb.sunysb.edu/~marat/SAM.html>. We thank Marat Khairoutdinov for  
476 maintaining the SAM code and Peter Blossey for helping with setting up the ASTEX case.

477

478 **Reference:**

- 479 Agee, E. M. (1987). Mesoscale cellular convection over the oceans. *Dynamics of atmospheres*  
480 *and oceans*, 10(4), 317-341.
- 481 Albrecht, B. A., Bretherton, C. S., Johnson, D., Schubert, W. H., & Frisch, A. S. (1995). The  
482 Atlantic stratocumulus transition experiment—ASTEX. *Bulletin of the American*  
483 *Meteorological Society*, 76(6), 889-904.
- 484 Bretherton, C. S., & Blossey, P. N. (2014). Low cloud reduction in a greenhouse-warmed  
485 climate: Results from Lagrangian LES of a subtropical marine cloudiness transition.  
486 *Journal of Advances in Modeling Earth Systems*, 6(1), 91-114.
- 487 Bretherton, C. S., Uchida, J., & Blossey, P. N. (2010). Slow manifolds and multiple equilibria in  
488 stratocumulus-capped boundary layers. *Journal of Advances in Modeling Earth Systems*,  
489 2(4).
- 490 Bretherton, C. S., & Wyant, M. C. (1997). Moisture transport, lower-tropospheric stability, and  
491 decoupling of cloud-topped boundary layers. *Journal of the Atmospheric Sciences*, 54(1),  
492 148-167.
- 493 Caldwell, P., & Bretherton, C. S. (2009). Response of a subtropical stratocumulus-capped mixed  
494 layer to climate and aerosol changes. *Journal of Climate*, 22(1), 20-38.
- 495 Caldwell, P., Bretherton, C. S., & Wood, R. (2005). Mixed-layer budget analysis of the diurnal  
496 cycle of entrainment in southeast Pacific stratocumulus. *Journal of the Atmospheric*  
497 *Sciences*, 62(10), 3775-3791.
- 498 Fletcher, J. K., Mason, S., & Jakob, C. (2016). A climatology of clouds in marine cold air  
499 outbreaks in both hemispheres. *Journal of Climate*, 29(18), 6677-6692.

500 Goren, T., Rosenfeld, D., Sourdeval, O., & Quaas, J. (2018a). Satellite Observations of  
501 Precipitating Marine Stratocumulus Show Greater Cloud Fraction for Decoupled Clouds  
502 in Comparison to Coupled Clouds. *Geophysical Research Letters*, 0(0).  
503 <https://agupubs.onlinelibrary.wiley.com/doi/abs/10.1029/2018GL078122>

504 Goren, T., Rosenfeld, D., Sourdeval, O., & Quaas, J. (2018b). Satellite observations of  
505 precipitating marine stratocumulus show greater cloud fraction for decoupled clouds in  
506 comparison to coupled clouds. *Geophysical Research Letters*.

507 Hahn, C. J., & Warren, S. G. (2007). *A gridded climatology of clouds over land (1971-96) and*  
508 *ocean (1954-97) from surface observations worldwide.*

509 Hartmann, D. L., Ockert-Bell, M. E., & Michelsen, M. L. (1992). The effect of cloud type on  
510 Earth's energy balance: Global analysis. *Journal of Climate*, 5(11), 1281-1304.

511 Holton, J. R. (1973). An introduction to dynamic meteorology. *American Journal of Physics*,  
512 41(5), 752-754.

513 Iacono, M. J., Delamere, J. S., Mlawer, E. J., Shephard, M. W., Clough, S. A., & Collins, W. D.  
514 (2008). Radiative forcing by long-lived greenhouse gases: Calculations with the AER  
515 radiative transfer models. *Journal of Geophysical Research: Atmospheres*, 113(D13).

516 Jones, C., Bretherton, C., & Blossey, P. (2014). Fast stratocumulus time scale in mixed layer  
517 model and large eddy simulation. *Journal of Advances in Modeling Earth Systems*, 6(1),  
518 206-222.

519 Khairoutdinov, M., & Kogan, Y. (2000). A new cloud physics parameterization in a large-eddy  
520 simulation model of marine stratocumulus. *Monthly Weather Review*, 128(1), 229-243.

521 Khairoutdinov, M. F., & Randall, D. A. (2003). Cloud resolving modeling of the ARM summer  
522 1997 IOP: Model formulation, results, uncertainties, and sensitivities. *Journal of the*  
523 *Atmospheric Sciences*, 60(4), 607-625.

524 Klein, S. A., Hall, A., Norris, J. R., & Pincus, R. (2017). Low-cloud feedbacks from cloud-  
525 controlling factors: a review. In *Shallow Clouds, Water Vapor, Circulation, and Climate*  
526 *Sensitivity* (pp. 135-157): Springer.

527 Lilly, D. K. (1968). Models of cloud-topped mixed layers under a strong inversion. *Quarterly*  
528 *Journal of the Royal Meteorological Society*, 94(401), 292-309.

529 Mahrt, L. (2014). Stably stratified atmospheric boundary layers. *Annual Review of Fluid*  
530 *Mechanics*, 46, 23-45.

531 Miller, M. A., & Albrecht, B. A. (1995). Surface-based observations of mesoscale cumulus-  
532 stratocumulus interaction during ASTEX. *Journal of the Atmospheric Sciences*, 52(16),  
533 2809-2826.

534 Moeng, C.-H., & Rotunno, R. (1990). Vertical-velocity skewness in the buoyancy-driven  
535 boundary layer. *Journal of the Atmospheric Sciences*, 47(9), 1149-1162.

536 Myers, T. A., & Norris, J. R. (2015). On the relationships between subtropical clouds and  
537 meteorology in observations and CMIP3 and CMIP5 models. *Journal of Climate*, 28(8),  
538 2945-2967.

539 Naud, C.M., Booth, J.F., Protat, A., Lamer, K., Marchand, R. and McFarquhar, G.M., Boundary  
540 Layer Cloud Controlling Factors in the Midlatitudes: Southern versus Northern Ocean  
541 Clouds. In *AGU Fall Meeting 2020*. AGU.

542 Nicholls, S. (1984). The dynamics of stratocumulus: Aircraft observations and comparisons with  
543 a mixed layer model. *Quarterly Journal of the Royal Meteorological Society*, 110(466),  
544 783-820.

545 Nicholls, S., & Leighton, J. (1986). An observational study of the structure of stratiform cloud  
546 sheets: Part I. Structure. *Quarterly Journal of the Royal Meteorological Society*, 112(472),  
547 431-460.

548 Norris, J. R., & Iacobellis, S. F. (2005). North Pacific cloud feedbacks inferred from synoptic-  
549 scale dynamic and thermodynamic relationships. *Journal of Climate*, 18(22), 4862-4878.

550 Norris, J. R., & Klein, S. A. (2000). Low cloud type over the ocean from surface observations.  
551 Part III: Relationship to vertical motion and the regional surface synoptic environment.  
552 *Journal of Climate*, 13(1), 245-256.

553 Petty, G. W. (2006). *A first course in atmospheric radiation*: Sundog Pub.

554 Romps, D. M. (2017). Exact Expression for the Lifting Condensation Level. *Journal of the*  
555 *Atmospheric Sciences*, 74(12), 3891-3900.

556 Sandu, I., & Stevens, B. (2011). On the factors modulating the stratocumulus to cumulus  
557 transitions. *Journal of the Atmospheric Sciences*, 68(9), 1865-1881.

558 Schubert, W. H., Wakefield, J. S., Steiner, E. J., & Cox, S. K. (1979a). Marine stratocumulus  
559 convection. Part I: Governing equations and horizontally homogeneous solutions.  
560 *Journal of the Atmospheric Sciences*, 36(7), 1286-1307.

561 Schubert, W. H., Wakefield, J. S., Steiner, E. J., & Cox, S. K. (1979b). Marine stratocumulus  
562 convection. Part II: Horizontally inhomogeneous solutions. *Journal of Atmospheric*  
563 *Sciences*, 36(7), 1308-1324.

564 Scott, R. C., Myers, T. A., Norris, J. R., Zelinka, M. D., Klein, S. A., Sun, M., & Doelling, D. R.  
565 (2020). Observed Sensitivity of Low Cloud Radiative Effects to Meteorological  
566 Perturbations over the Global Oceans. *Journal of Climate*.

567 Smolarkiewicz, P. K., & Grabowski, W. W. (1990). The multidimensional positive definite  
568 advection transport algorithm: Nonoscillatory option. *Journal of Computational Physics*,  
569 86(2), 355-375.

570 Stevens, B. (2006). Bulk boundary-layer concepts for simplified models of tropical dynamics.  
571 *Theoretical and Computational Fluid Dynamics*, 20(5-6), 279-304.

572 Stevens, B., Cotton, W. R., Feingold, G., & Moeng, C.-H. (1998). Large-eddy simulations of  
573 strongly precipitating, shallow, stratocumulus-topped boundary layers. *Journal of the*  
574 *Atmospheric Sciences*, 55(24), 3616-3638.

575 Uchida, J., Bretherton, C., & Blossey, P. (2010). The sensitivity of stratocumulus-capped mixed  
576 layers to cloud droplet concentration: Do LES and mixed-layer models agree?  
577 *Atmospheric Chemistry and Physics*, 10(9), 4097-4109.

578 Van der Dussen, J., De Roode, S., Ackerman, A. S., Blossey, P. N., Bretherton, C. S., Kurowski,  
579 M. J., et al. (2013). The GASS/EUCLIPSE model intercomparison of the stratocumulus  
580 transition as observed during ASTEX: LES results. *Journal of Advances in Modeling*  
581 *Earth Systems*, 5(3), 483-499.

582 Wakefield, J. S., & Schubert, W. H. (1981). Mixed-layer mode simulation of eastern North  
583 Pacific stratocumulus. *Monthly Weather Review*, 109(9), 1952-1968.

584 Wall, C. J., Hartmann, D. L., & Ma, P.-L. (2017). Instantaneous linkages between clouds and  
585 large-scale meteorology over the Southern Ocean in observations and a climate model.  
586 *Journal of Climate*, 30(23), 9455-9474.

587 Wood, R. (2007). Cancellation of aerosol indirect effects in marine stratocumulus through cloud  
588 thinning. *Journal of the Atmospheric Sciences*, 64(7), 2657-2669.

589 Wood, R. (2012). Stratocumulus clouds. *Monthly Weather Review*, 140(8), 2373-2423.

590 Wyngaard, J. (1987). A physical mechanism for the asymmetry in top-down and bottom-up  
591 diffusion. *Journal of the Atmospheric Sciences*, 44(7), 1083-1087.

592 Yamaguchi, T., & Randall, D. A. (2008). Large-eddy simulation of evaporatively driven  
593 entrainment in cloud-topped mixed layers. *Journal of the Atmospheric Sciences*, 65(5),  
594 1481-1504.

595 Zhang, Y., Stevens, B., & Ghil, M. (2005). On the diurnal cycle and susceptibility to aerosol  
596 concentration in a stratocumulus-topped mixed layer. *Quarterly Journal of the Royal  
597 Meteorological Society: A journal of the atmospheric sciences, applied meteorology and  
598 physical oceanography*, 131(608), 1567-1583.

599 Zheng, Y., & Li, Z. (2019). Episodes of Warm-Air Advection Causing Cloud-Surface  
600 Decoupling During the MARCUS. *Journal of Geophysical Research: Atmospheres*.

601 Zheng, Y., Rosenfeld, D., & Li, Z. (2018). The Relationships Between Cloud Top Radiative  
602 Cooling Rates, Surface Latent Heat Fluxes, and Cloud-Base Heights in Marine  
603 Stratocumulus. *Journal of Geophysical Research: Atmospheres*, 123(20), 11,678-611,690.

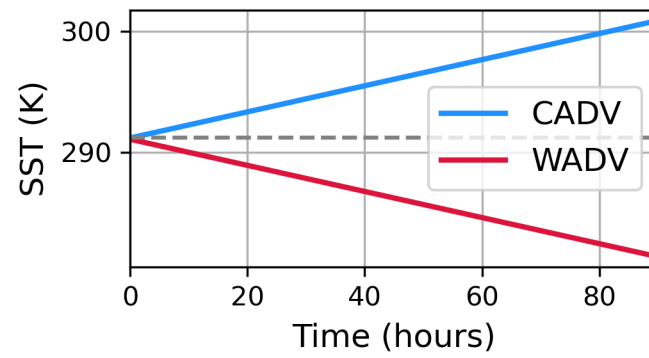
604 Zheng, Y., Rosenfeld, D., & Li, Z. (2020). A More General Paradigm for Understanding the  
605 Decoupling of Stratocumulus-Topped Boundary Layers: The Importance of Horizontal  
606 Temperature Advection. *Geophysical Research Letters*, 47(14), e2020GL087697.

607 Zheng, Y., Zhang, H., & Li, Z. (2020). Role of surface latent heat flux in shallow cloud  
608 transitions: A mechanism-denial LES study. *Earth and Space Science Open Archive  
609 ESSOAr*.

610

611

612 **Figures:**

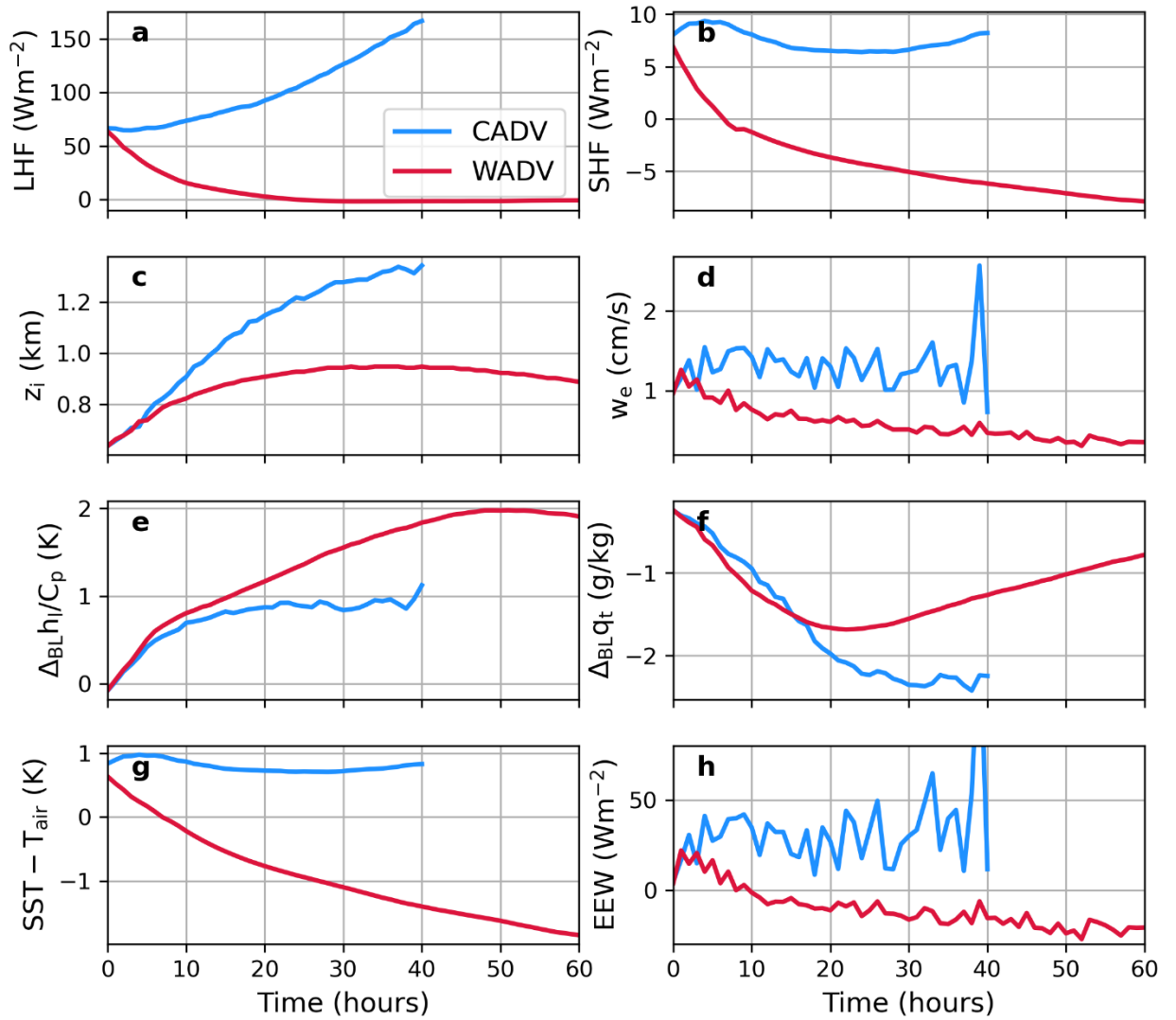


613

614 Figure 1: Time evolution of the sea surface temperature in the two simulations.

615

616



617

618

Figure 2: Time series of key variables of experiments CADV (blue) and WADV (red).

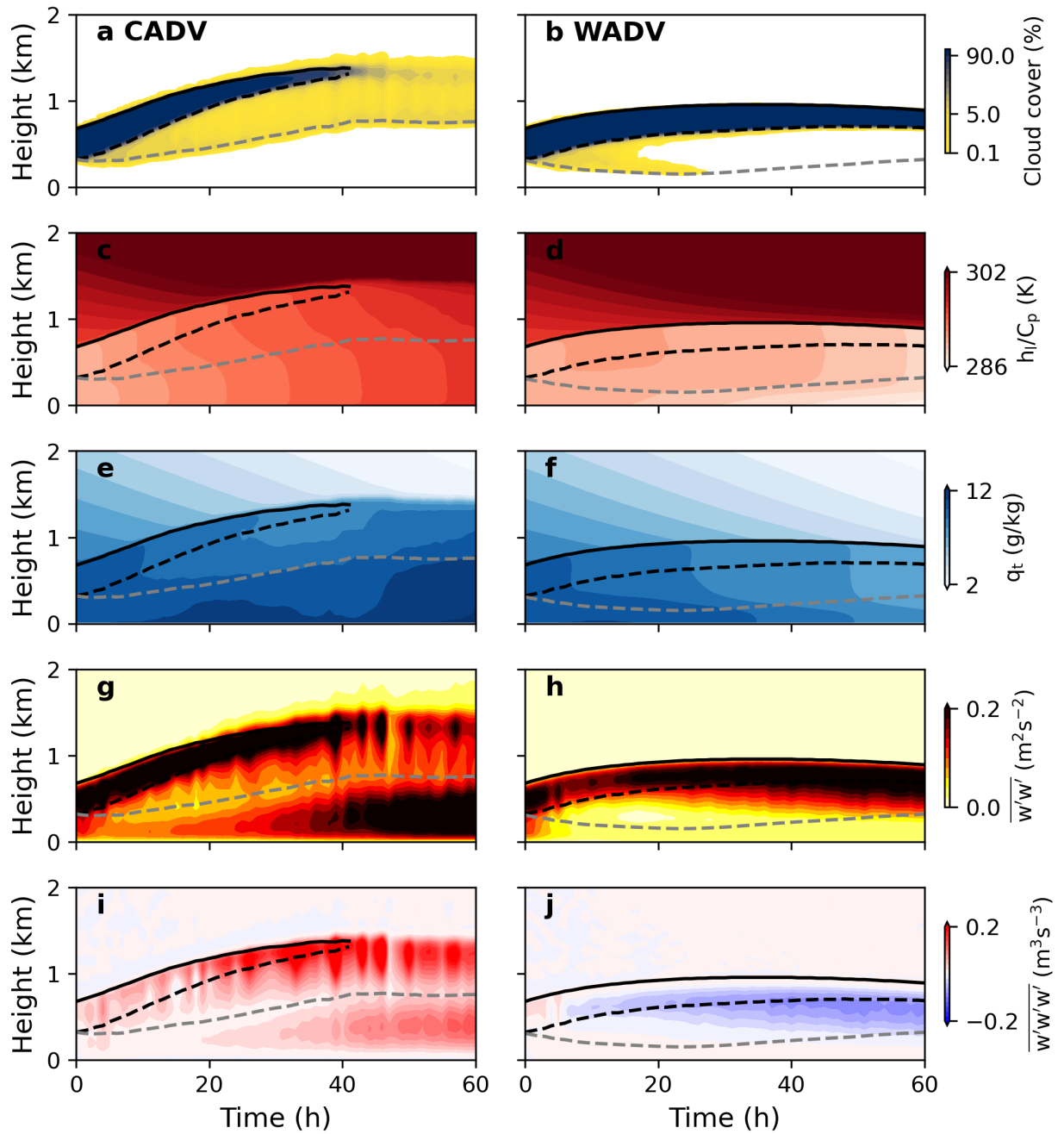
619

620

621

622

623



624

625

Figure 3: Time-height plots of key variables of experiments CADV (left) and WADV

626

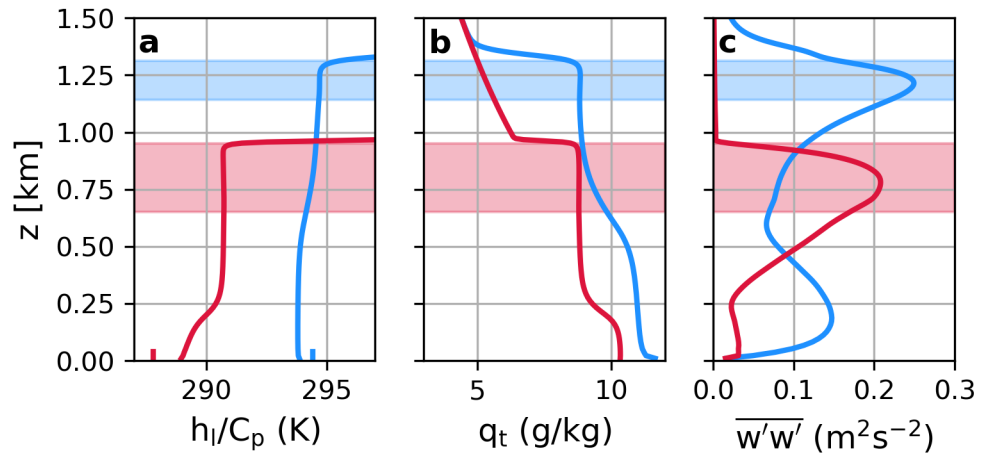
(right).

627

628

629

630



631

632 Figure 4: Profiles of  $h_l/C_p$  (a),  $q_t$  (b), and vertical velocity variance (c) for CADV (blue) and

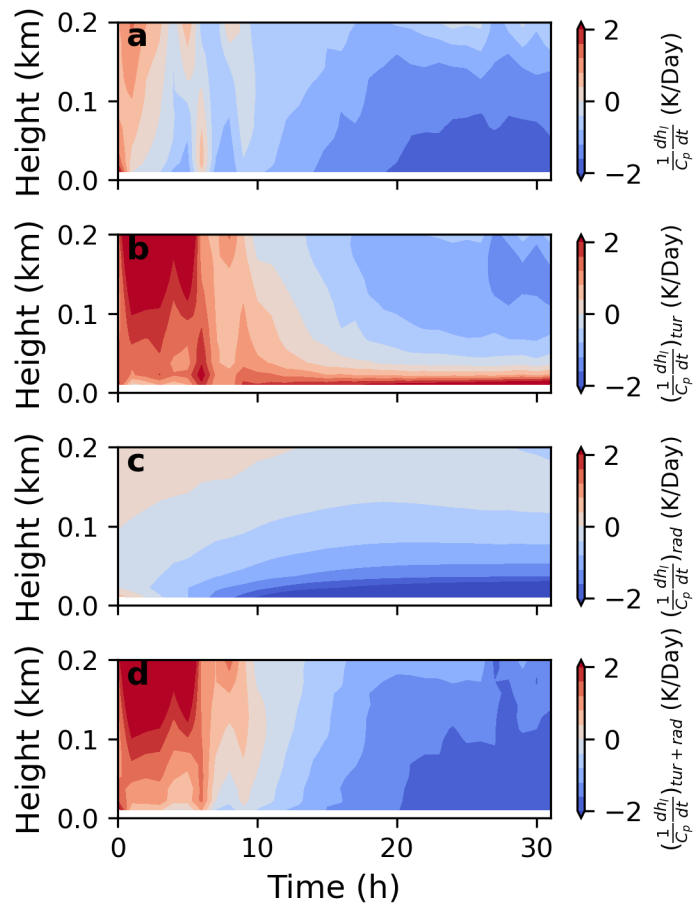
633 WADV (red) at  $t = 30$  h. Ticks at the bottom of (a) are the sea surface temperatures.

634

635

636

637



638

639 Figure 5: Time-height plots of total heating rate (a), heating rate due to turbulence (b),  
 640 heating rate due to radiation (c), and heating rate due to turbulence and radiation (d) for WADV.

641

642

643

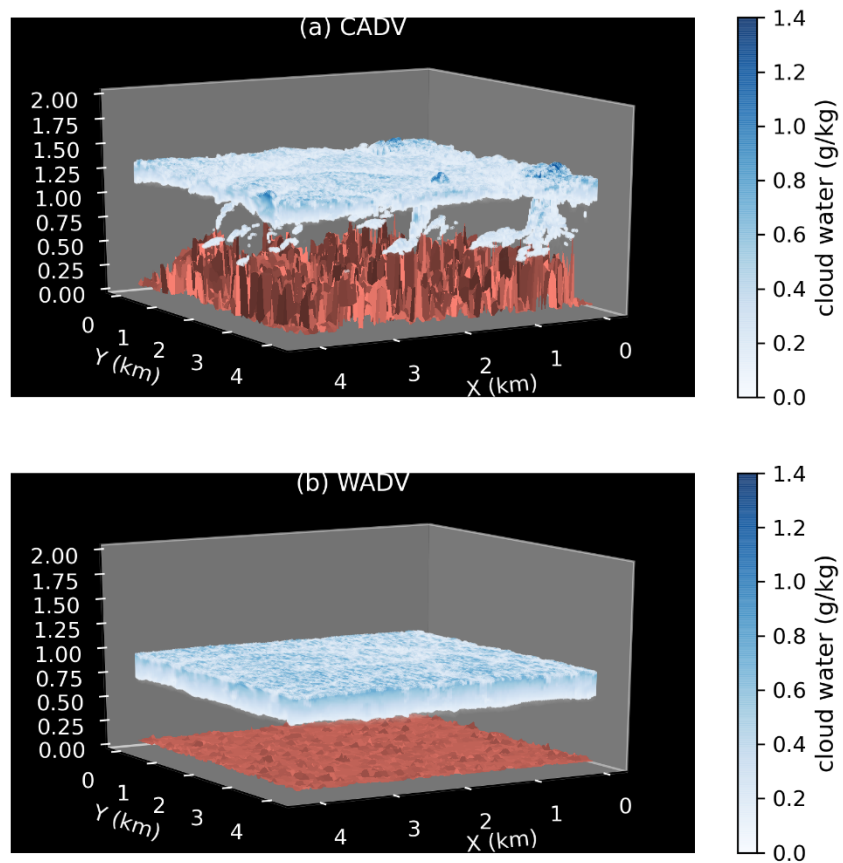
644

645

646

647

648



649

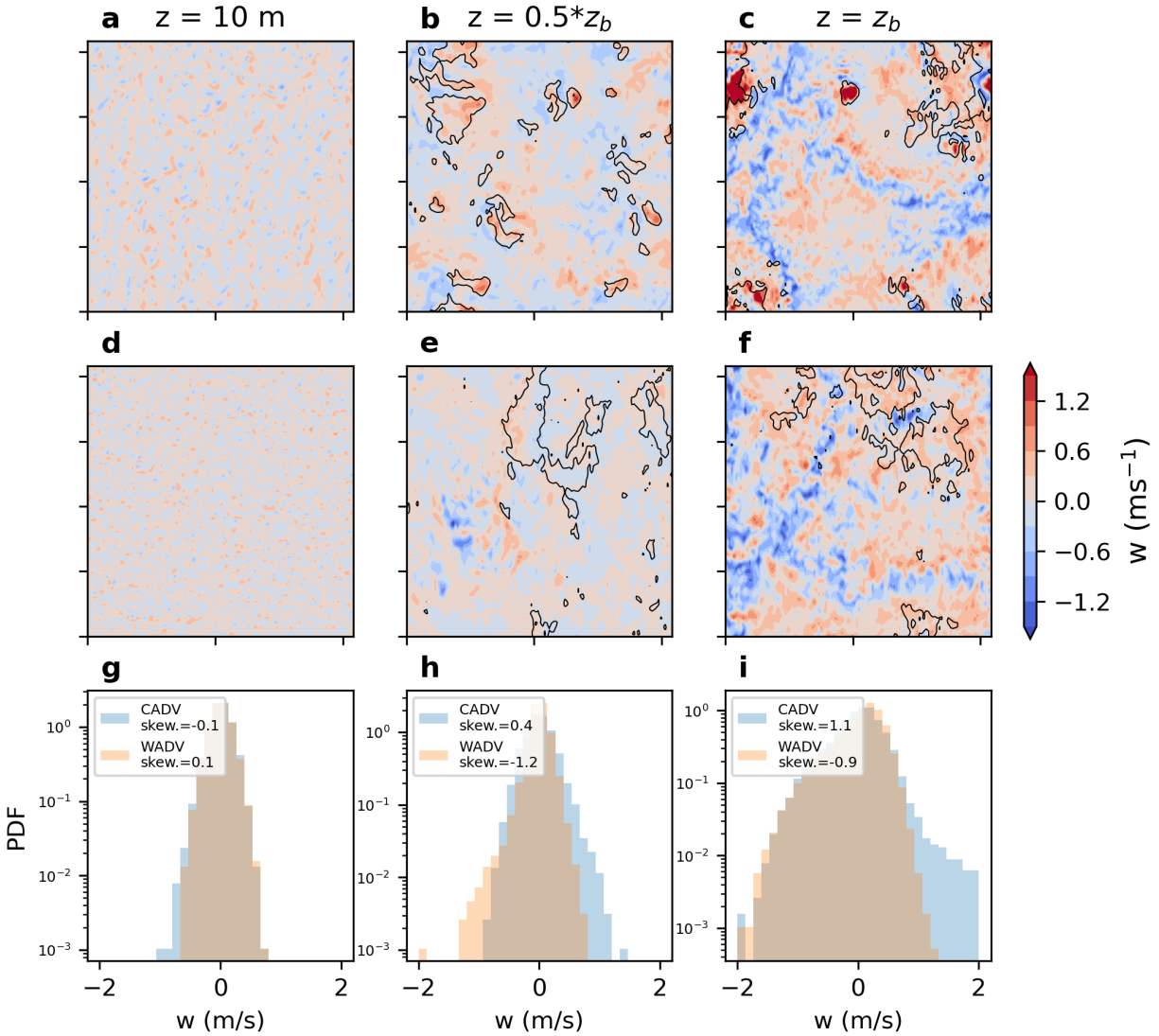
650 Figure 6: 3D visualizations of cloud liquid water content at  $t = 30$  h for the CADV and WADV

651 experiments. The red surfaces are the contours of the top 1%  $q_t$  in each column.

652

653

654

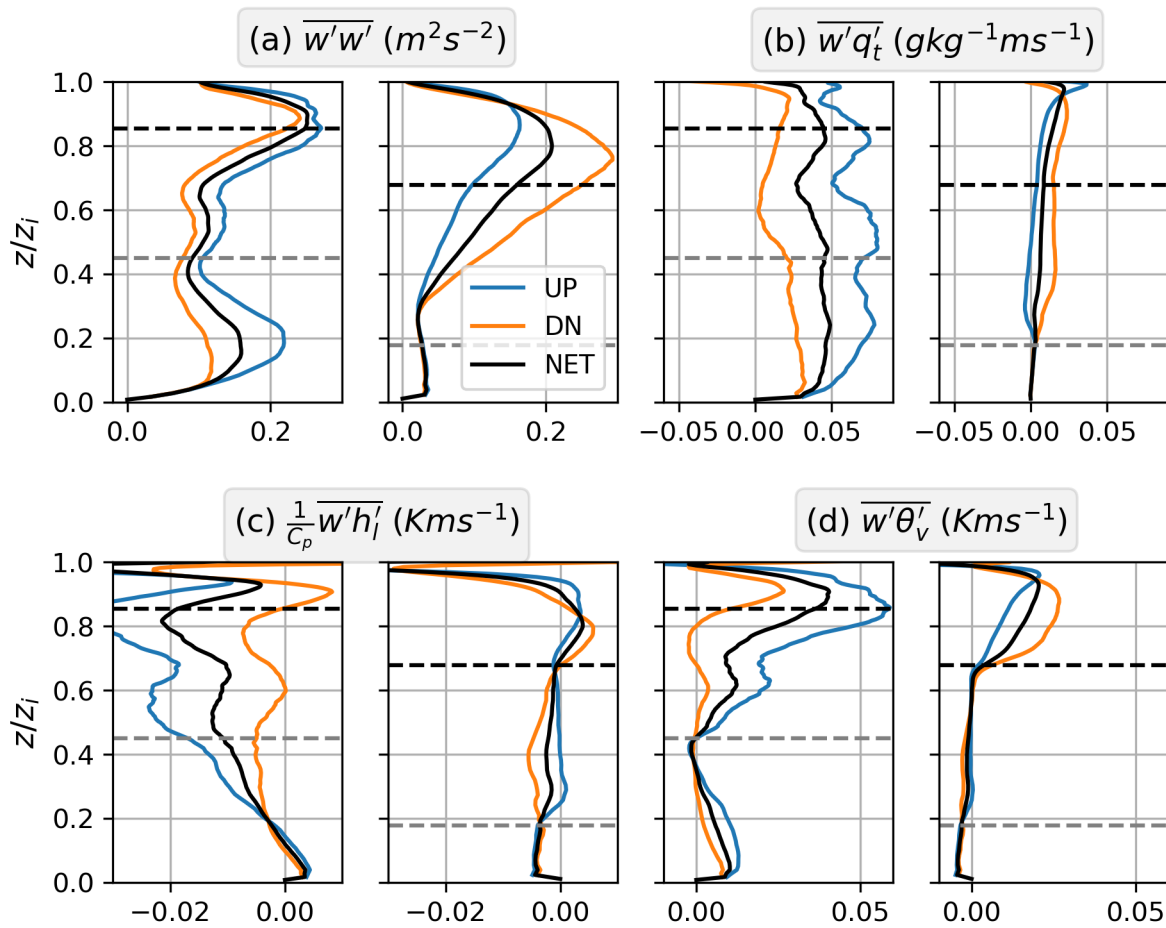


655

656 Figure 7: Vertical velocity field at  $z = 10\text{ m}$  (left),  $z = 0.5z_b$  (middle), and  $z = z_b$  (right) for the  
 657 CADV (top) and WADV (middle). The bottom panel is the probability distribution functions of  
 658 the vertical velocity for the two experiments. In (b), (c), (e), and (f), black contours correspond to  
 659 the top 10%  $q_t$  in each horizontal layer.

660

661



663

664 Figure 8: Vertical profiles of vertical velocity variance (a), moisture flux (b), heat flux (c), and  
 665 buoyancy flux (d) of updrafts (blue) and downdrafts (orange) for CADV (left) and WADV  
 666 (right). Horizontal black and grey dashed lines mark the base heights of stratocumulus decks and  
 667 LCL, respectively.

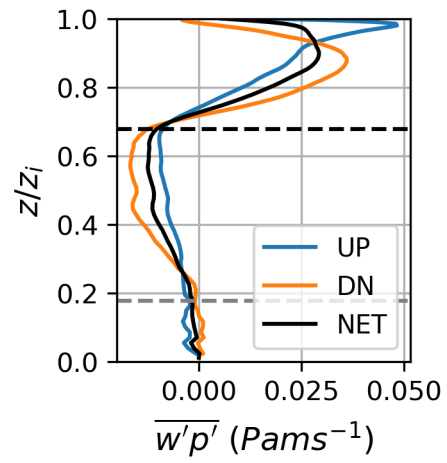
668

669

670

671

672



673

674

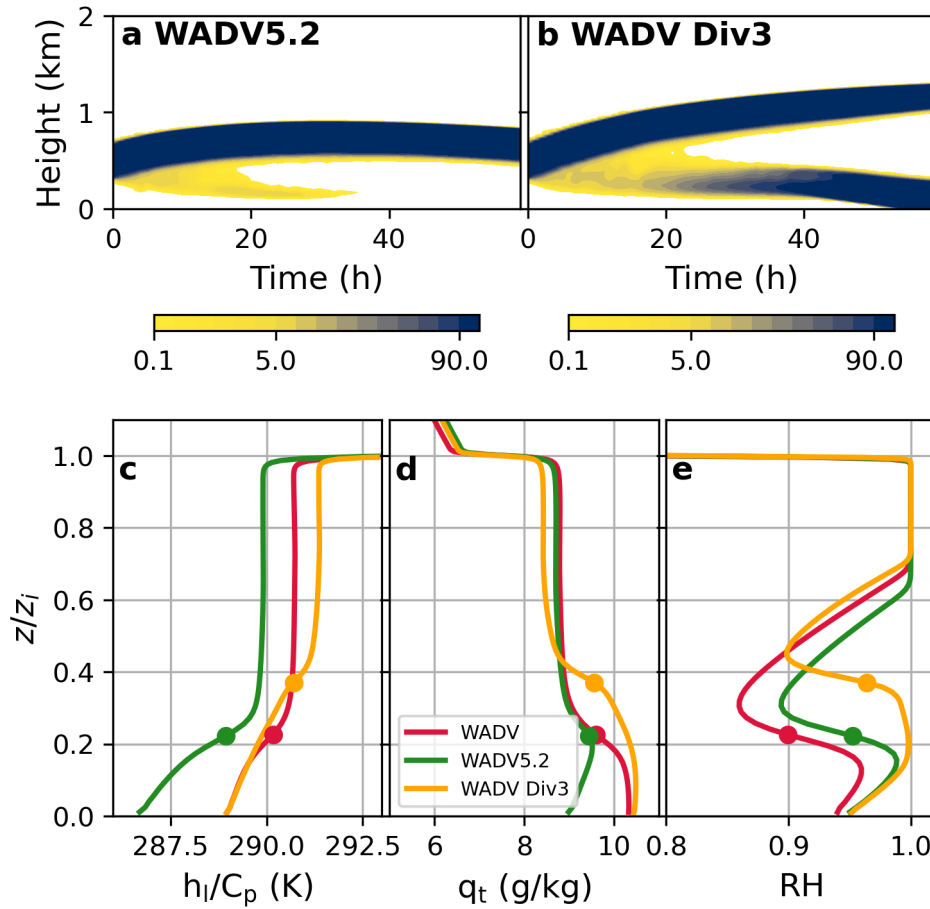
Figure 9: Vertical profiles of  $\overline{w'p'}$  at  $t = 30$  h in WADV.

675

676

677

678



679

680

681

682

683

684

685

686

687

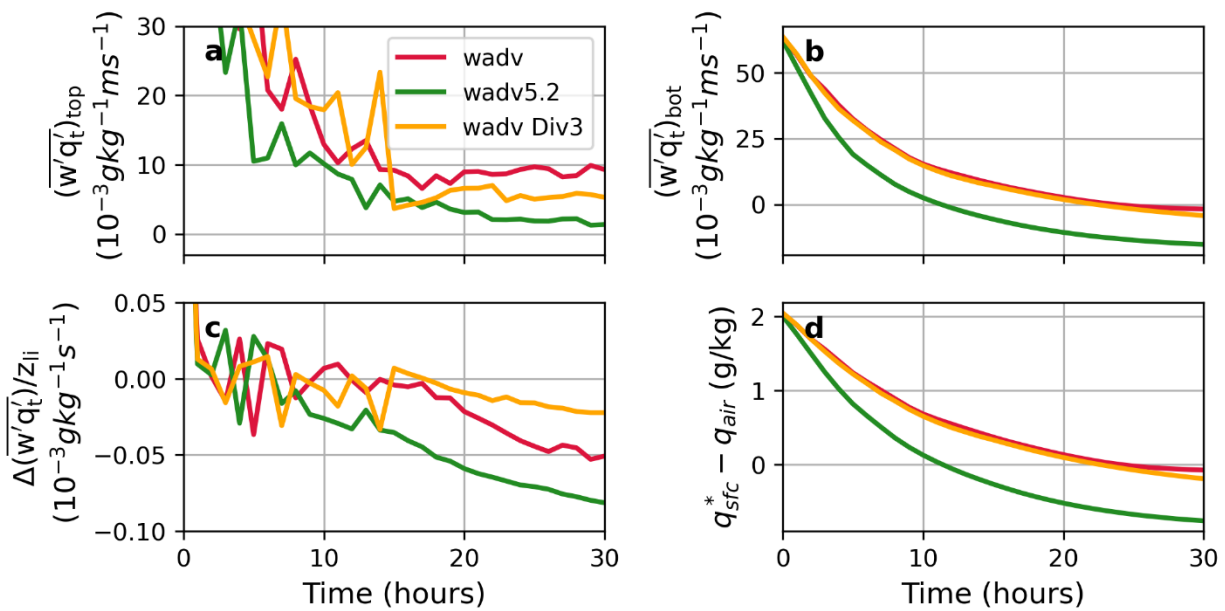
Figure 10: Time-height plots of cloud fraction for WADV5.2 (a) and WADV Div3 (b), and vertical profiles of  $h_l/C_p$  (c),  $q_t$  (d), and relative humidity (e) for the WADV, WADV5.2, and WADV Div3. The solid dots mark the  $z_{li}$ .

688

689

690

691



692

693 Figure 11: Time series of  $\overline{(w'q_t)_{top}}$  (a),  $\overline{(w'q_t)_{bot}}$  (b),  $(\overline{(w'q_t)_{top}} - \overline{(w'q_t)_{bot}})/z_{li}$  (c),  $q_{sfc}^* - q_{air}$

694

(d) for the three WADV runs.

695